

Communication and Sensing Applications of Six-Port Technology

Serioja O. Tatu¹, Ke Wu²

Abstract – A short review of the six-port theory and techniques for communication and sensing applications, such as signal-related down-conversion, direct modulation, and direction finding techniques, is presented in this paper. Six-port circuits have been fabricated in various technologies, covering a wide range of microwave and millimetre-wave frequencies. The paper illustrates and examines some relevant implementations over the last decade. In addition, circuit characterisation method using accurate network analyser and on-wafer measurements are described in details. Measurement results of various passive circuits from a novel power-divider to a V-band six-port circuit are discussed, demonstrating very good S-parameter and q_i point performances. To conclude this paper, system measurements of a Ka-band six-port direct conversion receiver and of an E-band six-port heterodyne FMCW radar are presented and discussed.

Keywords – Six-port technique, down-conversion, direct modulation, direction finding, radar sensor, millimetre-waves.

I. INTRODUCTION

The six-port circuit theory was initially developed in the 1970's for accurate low-cost measurements of the complex reflection coefficient in microwave network analysis [1] – [3]. During that period, vector network analyser was not available yet to tackle such measurement problems.

Since 1993, the six-port techniques were further expanded in function and developed for direct modulation or demodulation of microwave and millimetre-wave signals. Several six-port architectures for specific applications, such as high speed wireless communications or radar sensors, have been implemented and demonstrated.

Basically, the six-port acts as an interferometer; its output signals are linear combinations of input signals, conditioned by signal phases. This paper presents, for the first time, the use of identical six-port architecture for forming the transmitter and receiver stages of transceivers. Only the modules connected to its ports change the role played by the six-port (from quadrature modulator to homodyne or heterodyne down-conversion or direction finding circuit). The main difference versus its initial application as reflectometer is the addition of a fourth q_i point, which allows for a straightforward correspondence with the complex plane.

¹Serioja O. Tatu is with the «Institut national de la recherche scientifique - Énergie, Matériaux et Télécommunications», 800 rue de la Gauchetière Ouest, R 6900, Montréal, Québec, H5A1K6, Canada, E-mail: tatu@emt.inrs.ca

²Ke Wu is with the Poly-Grames Research Center, École Polytechnique de Montréal, Pavillon Lassonde, 2500, Chemin Polytechnique, Montréal, Québec, H3T1J4, Canada, E-mail: ke.wu@polymtl.ca

II. SIX-PORT CIRCUIT

As originally designed for automated measurements of the complex reflection coefficient, the six-port has a local oscillator input, a measurement port, and four outputs [3]. One of the outputs is used as a reference power level, and powers measured at the other ones are a function of the complex coefficient of the device under test connected to the measurement port. There are three different reflection coefficient values, named q_i points, which minimize the power at the corresponding i output. The ideal architecture requests that q_i points are spaced by 120° and are located equidistantly from the origin of the complex plane.

The new application fields require a different architecture of the circuit and new modules to be connected at its ports. Our approach is to design broadband six-port circuits, in order to avoid calibration procedures. This will dramatically increase data-rates up to quasi-optical speeds and will make possible the use of the circuit in a wider frequency range. The targeted performances in terms of S-parameters are the same.

A typical circuit is illustrated in Fig.1. It uses three 90° hybrid couplers and a power divider. The power divider is often replaced by a fourth 90° hybrid coupler with a 90° phase shifter connected at the direct port [4]. The isolated port of this coupler must be connected to a matched load.

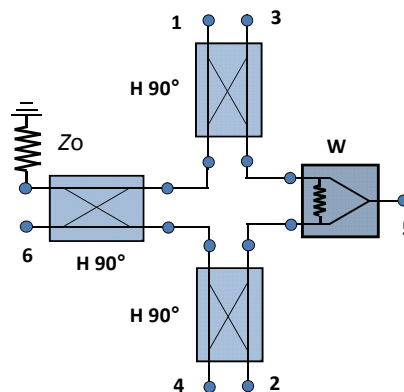


Fig. 1. Typical six-port architecture for communications and sensing

According to Fig.1, the S-parameter matrix of the circuit can be expressed by the Eq. (1).

In order to compute the S-parameter of the six-port circuit, we consider that the S-matrix of the 90° hybrid coupler and Wilkinson power divider are, respectively, expressed by Eqs. (2) and (3).

$$[S] = \frac{1}{2} \begin{bmatrix} 0 & 0 & 0 & 0 & -j & j \\ 0 & 0 & 0 & 0 & 1 & j \\ 0 & 0 & 0 & 0 & 1 & 1 \\ 0 & 0 & 0 & 0 & -j & -1 \\ -j & 1 & 1 & -j & 0 & 0 \\ j & j & 1 & -1 & 0 & 0 \end{bmatrix} \quad (1)$$

$$[S] = \frac{1}{\sqrt{2}} \begin{bmatrix} 0 & j & 1 & 0 \\ j & 0 & 0 & 1 \\ 1 & 0 & 0 & j \\ 0 & 1 & j & 0 \end{bmatrix} \quad (2)$$

$$[S] = \frac{-j}{\sqrt{2}} \begin{bmatrix} 0 & 1 & 1 \\ 1 & 0 & 0 \\ 1 & 0 & 0 \end{bmatrix} \quad (3)$$

The S-parameter matrix of the six-port circuit reveals that there are two clusters of ports, 1 to 4 and, 5 and 6. Inside each cluster, all the ports are perfectly matched and isolated one versus the others. In all applications they play separate functions, such as: four outputs and respectively two RF inputs for down-conversion, or four control inputs and RF output/input for direct modulators.

If the S-matrix is further analyzed, it is straightforward that if four matched loads are connected to the first group of ports (1 to 4) and two RF signals are applied to other pair of ports (5 and 6), all output signals (b_1 to b_4) are function of both inputs (a_5 and a_6). This is a fundamental difference, if compared to the six-port used in reflection coefficient measurements, where one of the outputs is used as a power reference [3].

In order to pursue the comparison, the q_i points can be also considered. We define these points as:

$$q_i = \frac{S_{i5}}{S_{i6}} \quad (4)$$

As illustrated in Fig. 2, the q_i points are: -1, -j, 1 and j; Eqs. (4) and (1) are used to compute these values.

The q_i points are spaced by 90° multiples and are located equidistantly from the origin of the complex plane. The phase difference between the pair of odd q_i points is 180° . The same result is obtained for the pair of even points.

A rotation of the q_i point's constellation in the complex plane is ensured by a phase shift of one of the RF ports. As an example, a clockwise rotation of 135° is obtained if a $3\lambda_g/8$ line is connected in series to the port 5 (see Fig. 3).

The q_i points are ideally positioned in the complex plane for modulation and demodulation purposes, as illustrated in next sections of the paper. The analysis of magnitude and phase errors of these points' position over the frequency will give to the designer an excellent tool to analyse the quality of such a circuit. For example, in the case of a direct demodulator, the magnitude errors will determine the number of signal levels

which can be easily detected. The phase errors will give the maximum number of symbols that can be disposed on a circle.

Our experience shows that the most robust modulations to be used in six-port based transceivers are, in order: BPSK, QPSK, 8 PSK, 16-star, and 32-star QAM. For this modulation schemes the symbols are placed on circles at minimum 45° phase shift one versus the other. The star modulations have an important advantage: the symbols are placed on concentrically equidistant circles, two for 16-star and four for 32-star QAM.

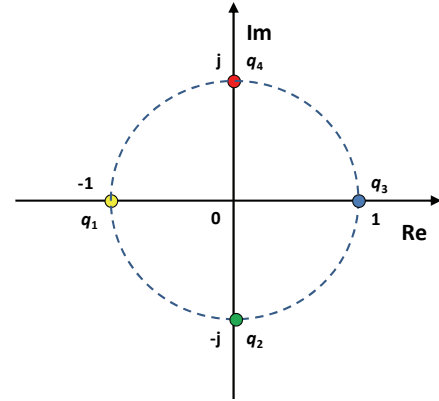


Fig. 2. The q_i points of the six-port

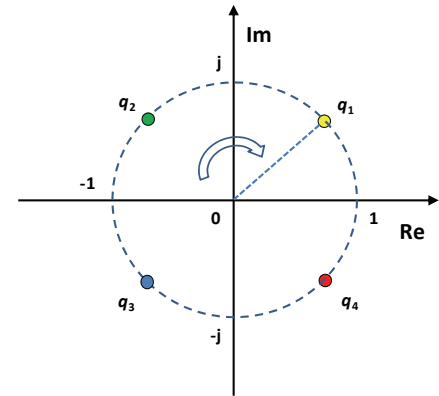


Fig. 3. The q_i points of the six-port (clockwise rotation)

III. DOWN-CONVERSION TECHNIQUES

The simplified block diagram of a typical six-port down-converter is plotted in Fig. 4. The local oscillator (LO) is connected at port 5 and the low noise amplifier (LNA) at port 6. Square-law matched power detectors are connected to the output ports of the circuit. The output signals are linear phase shifted combination of inputs, as seen in the same figure. Two differential amplifiers are used in order to obtain the output quadrature signals I and Q . The circuit can operate either in direct conversion or low intermediate frequency (IF) schemes.

If the input signals have amplitude ratio α , and different instantaneous frequencies and phases (as expressed by Eqs. (5) and (6)), we can compute the output signals [5].

$$a_5 = a \exp[j(\omega_0 t + \varphi_5)] \quad (5)$$

$$a_6 = \alpha(t) \cdot a \exp[j(\alpha t + \varphi_6(t))] \quad (6)$$

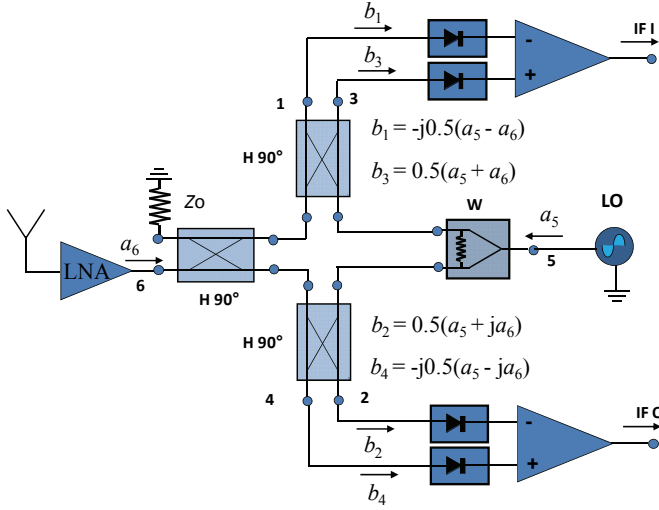


Fig. 4. Typical six-port front-end for quadrature down-conversion

$$v_{IF}^I(t) = \alpha(t)Ka^2 \cos[(\omega - \omega_0) \cdot t + (\varphi_6(t) - \varphi_5)] \quad (7)$$

$$v_{IF}^Q(t) = \alpha(t)Ka^2 \sin[(\omega - \omega_0) \cdot t + (\varphi_6(t) - \varphi_5)] \quad (8)$$

The quadrature down-conversion capability is therefore demonstrated. Constant value K is related to power detectors' efficiency and differential amplifiers' gain.

The previous equations show that the circuit can act also as a direct demodulator ($\omega = \omega_0$).

If the RF input signal is amplitude-modulated, the amplitude of quadrature signals is direct proportional with its amplitude. For a QAM signal the response of the demodulator versus the amplitude and phase variation of the RF input signal is linear.

We notice that, if the circuit is used as a low IF down-converter, a second in-phase down-conversion and low-pass filtering is required [5].

The same six-port circuit can also be used in quasi-conventional down-converter architecture, using anti-parallel diodes, as shown in Fig. 5. In this case, in order to keep the port numbers unchanged, the RF input signal is injected at port 5 and the LO is connected at port 6.

In addition, compared to the previous scheme, the non-linear characteristic approximation of the diode is considered:

$$I = cV + dV^2 + eV^3 \quad (9)$$

Two 90° phase shifters are used to ensure the required signals at the anti-parallel diode inputs. Therefore, b_2 and $-jb_4$ are the input signals in the first pair of diodes. The other pair of diodes is fed by $-jb_1$ and b_3 .

Due to the circuit symmetry, after intermodulation product filtering, the IF outputs will be in quadrature:

$$v_{IF}^Q(t) = jv_{IF}^I(t) \quad (10)$$

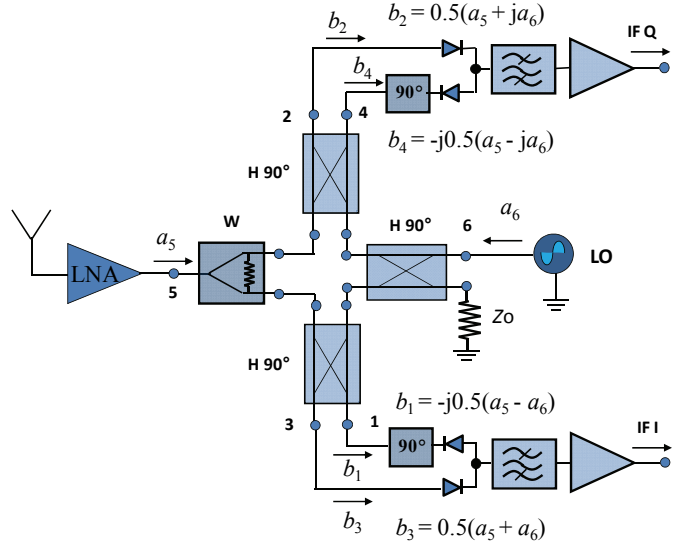


Fig. 5. Quasi-conventional six-port front-end for quadrature down-conversion

We notice the difference between the two down-conversion approaches.

In the first implementation, the diodes are optimized to operate as power detectors. The output spectrum contains only low IF and DC signals.

In the second one, due to the use of the whole non-linear characteristic of the diodes, the output spectrum is richer and must be carefully filtered. Therefore, in order to obtain comparable down-conversion results, the LO power must be considerably increased (with more than 20 dB) [6].

The typical implementation is recommended in communication transceivers, operating with a low LO power.

The second implementation can be an option if high LO power is available (for example in a radar sensor, as illustrated in next sections). A very good isolation between RF inputs is required, especially for the quasi-conventional architecture.

IV. DIRECT MODULATION TECHNIQUE

The six-port modulator uses the circuit presented in Fig. 1, together with two pairs of mono-ports, having controllable reflection coefficients. A simplified block diagram is plotted in Fig. 6. The normalised continuous wave (CW) signal passing through the top or bottom hybrid couplers, is multiplied by the 90° phase shifted input reflection coefficient of the corresponding mono-port. The output signal of the direct modulator combines these signals, as follows:

$$b_5 = 0.5(\Gamma_1 + j\Gamma_2) \cdot a_6 \quad (11)$$

Therefore, the phase and the amplitude of the normalized output signal are related to the mono-port return loss values. The direct modulation of the input RF signal is straightforward; the modulated constellation can be rotated in the IQ complex plane adding a constant phase shift.

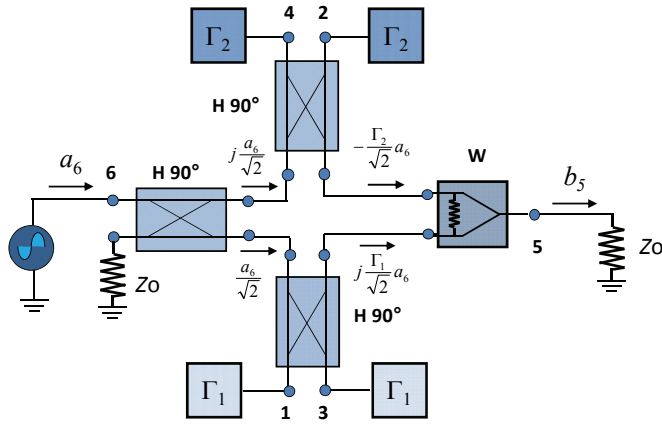


Fig. 6. Typical six-port direct modulator

The direct modulation technique is closely related to the six-port architecture and its four q_i points. Using only short or open circuit loads, the return loss values (Γ_1 and Γ_2) are equal to -1 and +1, respectively. A direct QPSK six-port modulator is obtained, according to the direct modulation chart presented in Table I.

TABLE I
QPSK DIRECT MODULATION CHART

Symbol	Gray code	Γ_1	Γ_2	Z_1	Z_2	b_5
1	00	1	1	∞	∞	$(1+j)a_6/2$
2	01	-1	1	0	∞	$(-1+j)a_6/2$
3	11	-1	-1	0	0	$(-1-j)a_6/2$
4	10	1	-1	∞	0	$(1-j)a_6/2$

It is to be noticed that all QAM or PSK modulation schemes can be implemented using the same technique. The challenge is to connect and commute the required loads with the symbol rate speed. This can be achieved using rapid switches (MEMS, PIN diodes...) controlled by a DSP module.

For example, the 8PSK modulation requires Γ_i values of 0, ± 1 , ± 0.707 , while a 16 QAM requires values of ± 0.25 and ± 0.75 [5].

The modulation schemes to be implemented are limited only by the imagination of the designer, the performances of the six-port, switching modules and related pairs of loads.

V. DIRECTION FINDING TECHNIQUE

A direction finding module can be designed using the same six-port circuit, two omnidirectional antennas, and two LNAs connected to the input RF ports, as shown in Fig. 7.

The six-port output signals are detected, amplified and processed according to Eqs. (7) and (8), while keeping in mind that $\omega = \omega_0$ because the two inputs receive the same signal (phase shifted). The baseband complex signal is used to find the RF signals' direction of arrival.

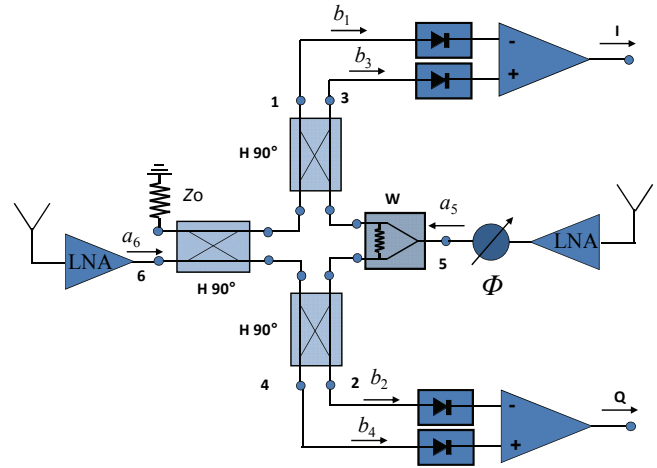


Fig. 7. Six-port direction finding front-end

The receiving omni-directional antennas are spaced by a distance d and the angle of arrival is equal to θ , as illustrated using a geometrical model in Fig. 8.

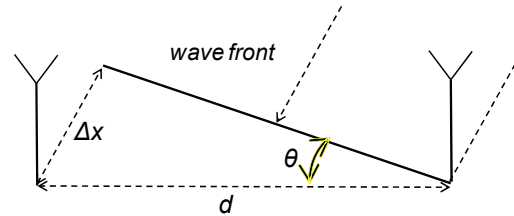


Fig. 8. Geometrical model for angle of arrival measurements

The phase difference between the input RF signals $\Delta\phi$ is related to the path difference Δx :

$$\Delta x = \lambda \frac{\Delta\phi}{2\pi} \quad (12)$$

The angle of arrival can be calculated as follows:

$$\sin \theta = \frac{\Delta x}{d} = \frac{\lambda}{d} \cdot \frac{\Delta\phi}{2\pi} \quad (13)$$

The two RF signals received by the antennas will be in-phase, if the path difference is zero or a whole number of wavelengths. In order to avoid any ambiguity, the distance between antennas, d , is chosen at a half of the wavelength. Hence, the angle of arrival can be computed as:

$$\sin \theta = \frac{\Delta\phi}{\pi} = \frac{1}{\pi} \arctg \frac{v_Q}{v_I} \quad (14)$$

The system is initially calibrated using the phase shifter; the quadrature voltage V_Q is minimized for $\theta = 0^\circ$.

If the antenna system can be rotated in the horizontal plane, this is a straightforward method to obtain the angle of arrival θ . If not, the Eq. (14) is used.

VI. FABRICATION TECHNOLOGIES

In the past 15 years, the six-port circuit has been designed, fabricated and characterised in a wide frequency spectrum, from 250 MHz up to 94 GHz and beyond, according to specific applications. A special attention was accorded to high microwave and millimetre-wave spectrum, due to emerging applications, such as ultra-high-speed wireless communications, automotive radar, and imaging sensors.

A wide-band (23 - 31 GHz) circuit has been fabricated in Miniaturized Hybrid Microwave Integrated Circuits (MHMICs) technology, on a 254 μm ceramic substrate with a relative permittivity $\epsilon_r = 9.9$. The chip measures 25.4 x 25.4 mm. The complete RF microstrip topology is shown in Fig. 9 and consists of a wide-band Ka band six-port junction with surface-mounted RF diodes and related matching circuit network [7].

For a further miniaturization, a Monolithic Microwave Integrated Circuit (MMIC) six-port module has been fabricated on a 100 μm TriQuint's GaAs substrate with a relative permittivity $\epsilon_r = 12.9$. Two different circuits, operating in the frequency range of 24 to 30 GHz, have been integrated using: (i) distributed element couplers and (ii) a combination of distributed and discrete components [8].

The distributed element implementation yields a relatively large size (4 x 4 mm), but it has excellent S-parameter performances. Power detectors are integrated on the chip. A photo of the MMIC circuit is shown in Fig. 10.

The hybrid implementation using high impedance transmission lines and capacities leads to an important size reduction (2 x 3 mm) keeping good S-parameter performances. To miniaturize the 90° hybrid couplers, higher characteristic impedance transmission lines are used, and shunt capacitors of 200 fF value are loaded near the ports. So, the diameter of this coupler becomes 600 μm compared with 1330 μm in the first MMIC design. The RF Schottky diode matching networks are also realized using the same technique. Fig. 11 shows the RF topology of this second MMIC circuit.

Higher frequency millimetre-wave circuits and fabrication technologies for prototyping have been further investigated.

In a first step, waveguide circuits were designed due to their facility to be interconnected to standard laboratory equipment.

Let us see an example of such six-port design. A combined Substrate Integrated Waveguide (SIW) and conventional rectangular waveguide (RWG) structure is the core of a 94 GHz radar sensor [9]. Fig. 12 shows the W-band SIW six-port, including the alumina part of the transitions to standard WR-10 RWG. The SIW six-port dimensions are 18.6 x 35.7 mm. The circuit, fabricated on 254 μm thick alumina, has been embedded in a brass structure, including, for the each port, a wave-guide stepped transition, as seen in Fig. 13. The brass fixture dimensions are 43 x 50 x 11 mm. Wave-guided mounted power detectors are connected to circuit outputs (1 to 4), to build a down-conversion module. Matched terminations are used for ports 7 and 8.

In order to reduce the size of circuits, the use of MHMICs technology has been also investigated for millimetre-wave circuits operating at the frequencies higher than 60 GHz.

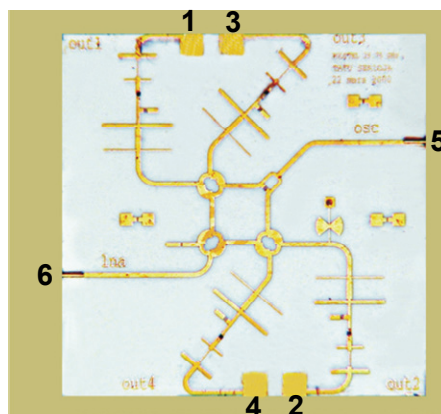


Fig. 9. Photograph of the MHMIC six-port module

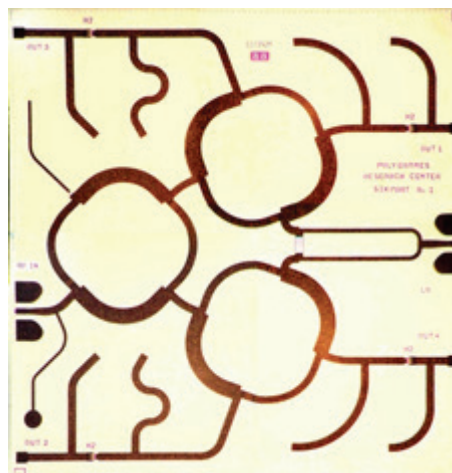


Fig. 10. Photograph of the MMIC six-port module

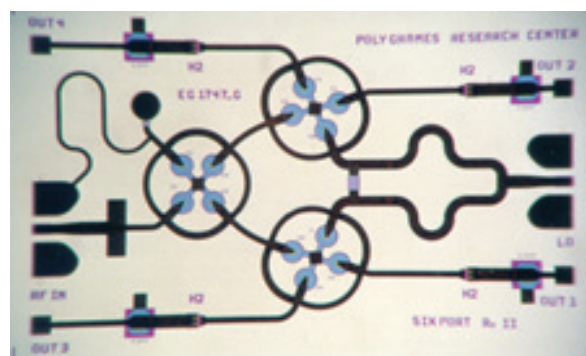


Fig. 11. Photograph of the reduced size MHMIC six-port module

As it is known, the width of the 50 Ω microstrip line for alumina is practically equal to the substrate thickness. The quarter wave line length is shortened compared to Ka-band design in Fig. 9. To operate higher frequencies, starting from V-band, the use of 254 μm thick alumina substrate is no longer possible due to the increased line width versus the quarter wavelength ratio.

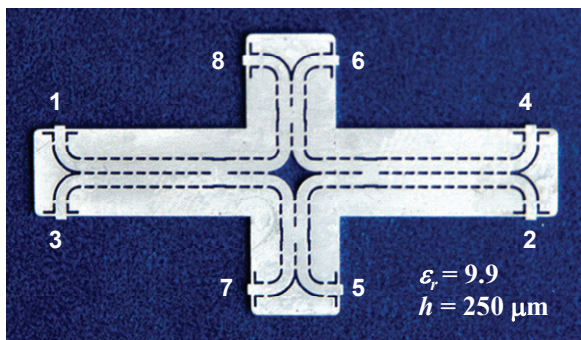


Fig. 12. Photograph of SIW six-port circuit

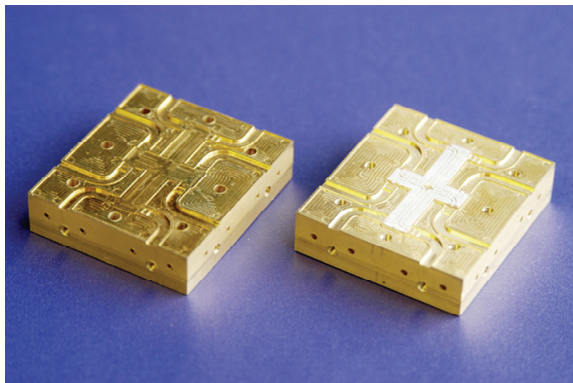


Fig. 13. Photograph of SIW six-port circuit in the brass fixture

Basic components, such as power dividers and couplers, require, therefore, a reduced thickness of alumina substrate, in order to keep this aspect ratio reasonable. Two methods are combined used: (i) an alumina substrate of 127 μm thick and (ii) the use of higher impedance transmission lines (thinner than that of regular 50 Ω microstrip lines), if necessary [10]. The circuits can be designed, for example, using 70.7 Ω and 50 Ω microstrip lines instead of 50 Ω and 35.36 Ω ones. Tapered transitions are used to connect 50 Ω circuits (such as integrated amplifiers or others devices).

In order to fabricate in-house low-cost prototypes, a combination of MHMIC, SIW, MMIC and RWG technologies has been used. SIW is a natural way to interconnect external waveguides with planar integrated circuits. The size of the RWG flange also copes with the size of MHMIC circuits.

A typical example of such fabrication is a 77 GHz radar sensor module [11]. Fig. 14 shows the receiver front-end, integrated into 127 microns thick alumina substrate (25.4 x 25.4 mm), and mounted in a brass fixture.

The receiver antenna array (Rx AA) is composed of eight patch antennas, having a measured gain of 12 dBi. The LNA chip, HMC-ALH509 of Hittite Corporation, is wire-bonded on MHMIC module using coplanar connections. The LNA is a three stage GaAs HEMT MMIC (71-86 GHz). It features 14 dB of gain and 5 dB of noise figure, with +2 V supply voltage (V_{dd}). The gate voltage (V_{gg}) is typically -0.2 V.

The six-port circuit architecture is similar with one presented in Fig. 5, quasi-conventional with anti-parallel Schottky diodes (type HSCH9161 of Agilent Technologies).

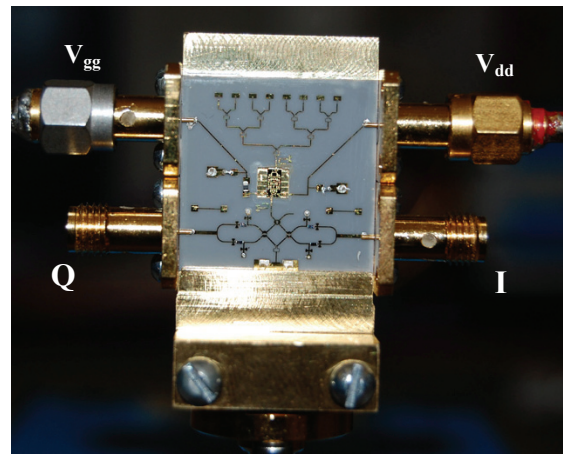


Fig. 14. Photograph of radar receiver front-end in the brass fixture

These Schottky devices are functional through W-band (110 GHz). The pins' width (120 μm) is almost equal to the 50 Ω line width on 127 μm alumina, making easier to provide a good matching network design and microstrip assembly.

SMA connectors are used for LNA DC bias (top) and quadrature outputs (bottom). A transition to WR 12 rectangular waveguide is also implemented (bottom) to ensure connectivity to standard equipment, which generates the millimetre-wave signal.

VII. CIRCUIT'S CHARACTERISATION TECHNIQUE

In the circuit characterisation process, two different measurement techniques are used.

The first one is the RWG technique. Characterisation and measurement of such circuits using the Vector Network Analyser (VNA) is facilitated by the use of RWG flanges and a standard RWG calibration kit. The devices under test (DUT) are equipped with RWG transitions to all ports. The unused ports are terminated by RWG matched loads. Hence, one single circuit is required for full S-parameter characterisation. A main disadvantage is the high fabrication cost, weight and size of prototypes. In addition, the measurement results are distorted by the transitions' mismatch and insertion loss.

The second technique is based on on-wafer measurements. Fig. 15 shows the millimetre-wave circuits' measurement set-up: the Agilent Technologies' E8362B Precision Network Analyzer (PNA), equipped with two OML millimetre-wave modules, and a Cascade Microtech 9000 probe station, equipped with two 3D precision positioners manufactured at Focus Microwaves. An Olympus stereo microscope with high resolution Infinity 1-5 CMOS camera and a large LCD display are used to capture and display images.

Fig. 16 shows a circuit under measurement using 150 μm ground-signal-ground (GSG) coplanar pico-probes, connected through standard WR-12 waveguides at the millimetre-wave modules of the PNA. The waveguide solution (instead of GSG probes connected by cables) was chosen to increase the dynamic range of the measurements and improve the calibration.



Fig. 15. S-parameter measurement set-up



Fig. 16. Circuit under measurement using pico-probes

In order to exemplify the on-wafer measurement technique, let us look at some circuits prepared for two-port measurements and a selection of typical S-parameter results.

Fig. 17 shows a typical MHMICs alumina substrate (25.4 x 25.4 mm) containing various circuits prepared for two port measurements. Because the probe tips are coplanar, in the case of microstrip circuit measurements, transitions from microstrip to coplanar wave guide are required. To avoid via holes, and ensure measurement repeatability, quarter wavelength open lines and “butterfly wings” open circuited sectors are used as millimetre-wave short-circuits. The MHMICs integrated resistors of 50 Ω and 100 Ω are fabricated on 100 Ω per square titanium thin layer.

In order to ensure fast and reliable measurements, the on-wafer calibration and measurement with pico-probes were adopted. In the measurements presented in this paper, the through-reflect-line (TRL) calibration technique is used. The reference plan is considered at the centre of the through standard. In microstrip technology at millimetre-wave frequencies, the open standard is desirable. The length of the line is related to the higher frequency to be measured.

In order to guarantee successful calibration before each measurement, due to the fragility of the very thin gold layer metallization (1 μm), multiple identical standards have been fabricated. Three different TRL standards can be identified in the MHMICs die photograph.

As seen in the same Fig. 17, a novel ring power divider, a hybrid coupler and a six-port circuit are prepared for S-parameter measurements. The squared metallization regions are used in the initial process of pico-probes alignment. The electrical contact and the mechanical pressure against the substrate must be balanced for all three probe tips (mechanical adjustments are performed before each calibration procedure). Three 50 Ω resistors with pads are also used to control titanium layer thickness over the substrate area.

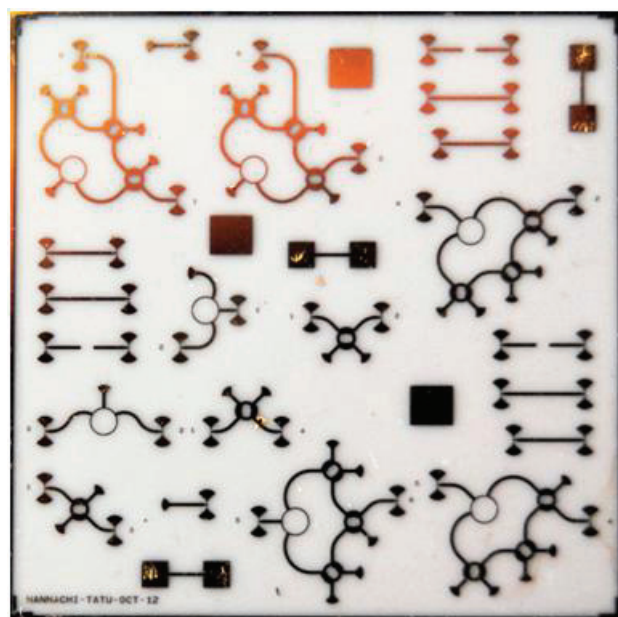


Fig. 17. Various MHMICs-based circuits on alumina

Fig. 18 shows the novel V-band ring power divider [12] prepared for transmission and isolation measurements. As already underlined, the third unused port is terminated by a 50 Ω load, to avoid reflections during two port measurements.



Fig. 18. Microphotograph of the novel ring power divider: S12 measurement configuration

Fig. 19 shows measurement results of the return loss and the outputs' isolation of the power divider, over a 5 GHz frequency band. The measurement results exhibit very good matching at all ports, while the isolation factor between the two output ports is at least 25 dB.

The transmission coefficient measurements of Fig. 20 show less than 0.25 dB of additional insertion loss over the considered band, while maintaining a quasi-null amplitude imbalance, which does not exceed 0.125 dB.

The measured phase performance of the circuit is illustrated in Fig. 21. The two outputs are in-phase, having less than 1° phase imbalance over the 5 GHz band.

The power divider is, therefore, optimal to be used as power splitter in a six-port.

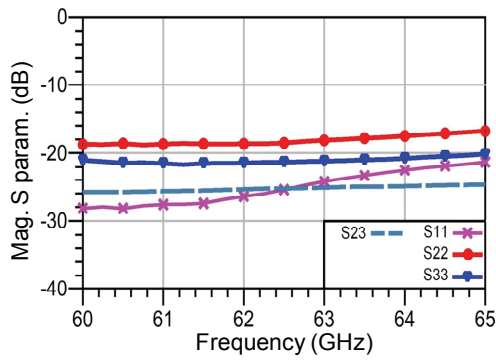


Fig. 19. Ring power divider: matching and isolation

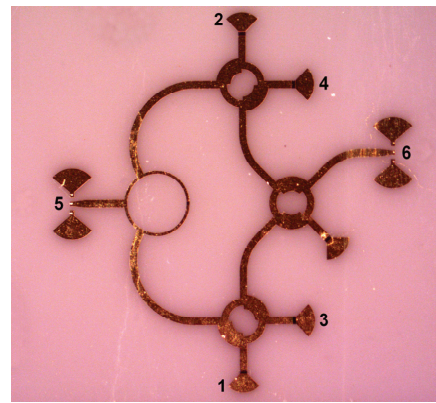


Fig. 22. Microphotograph of the V-band six-port

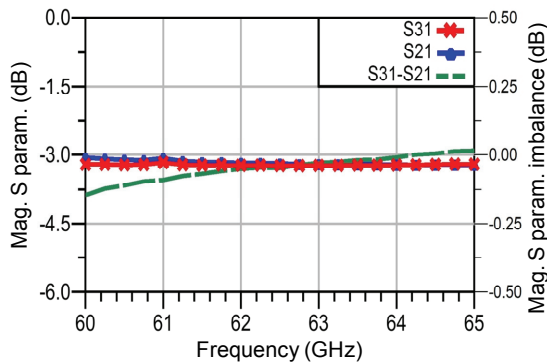


Fig. 20. Ring power divider: magnitude of transmission S parameter measurements

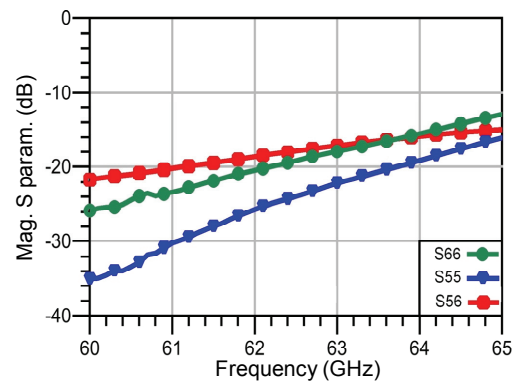


Fig. 23. Six-port: RF ports matching and isolation measurements

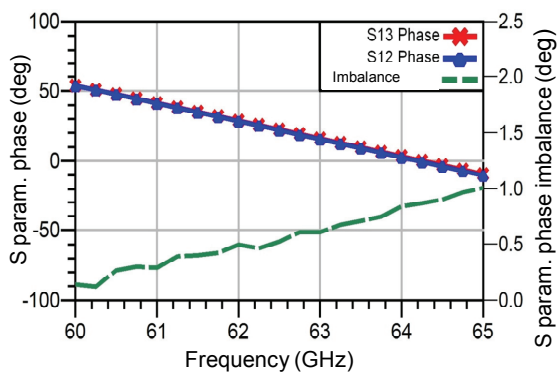


Fig. 21. Ring power divider: transmission phase measurements

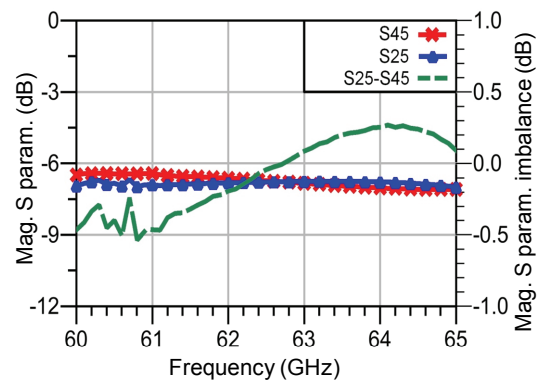


Fig. 24. Six-port: typical magnitude of transmission S parameters

Fig. 22 shows such a V-band six-port circuit prepared for RF port return loss and isolation measurements.

In Figs. 23 to 25 some typical S-parameter measurement results are presented. Very good return loss and isolation at RF ports are signalled in Fig. 23, and reduced magnitude imbalance of transmission S-parameters, in Fig. 24. Fig 25 shows a phase difference very close to 90° between signals transmitted from RF port 6 to ports 1 and 3. This result highlights the phase performance of the corresponding 90° hybrid coupler. The glitches observed in Figs. 25 and 26 in the beginning of the displayed frequency range are related to a PNA calibration error. To conclude our six-port analysis, the q_i points are plotted in Fig. 26. Very good performances in terms of magnitude and phase errors are revealed.

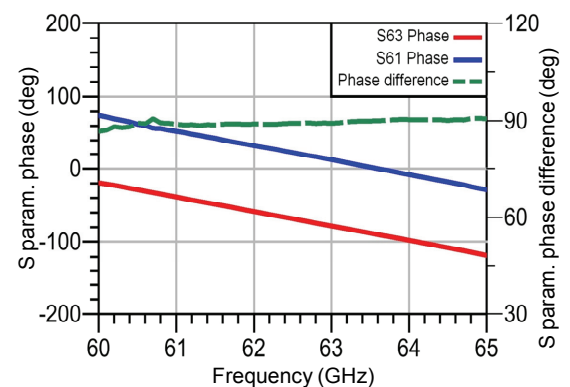


Fig. 25. Six-port: typical S parameters phase measurement

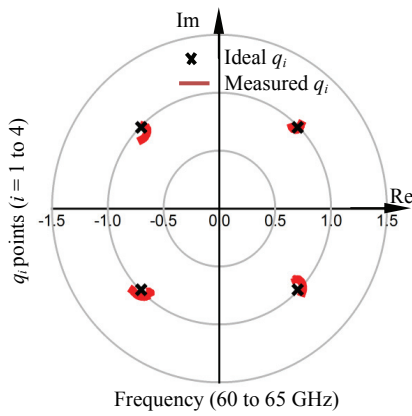


Fig. 26. Six-port: polar plot of the measured and ideal q_i points

VIII. SYSTEM MEASUREMENTS

System measurements are highly recommended to validate related system simulations and our in-house fabricated prototypes.

As a suggestive example, a Ka-band six-port receiver and E-band FMCW radar sensor using the receiver prototypes of Figs. 9 and 14, respectively, are considered [13], [14].

Fig. 27 shows the block diagram of the Ka-band direct conversion measurement set-up. The PSK/QAM modulated signal and the reference signal of 250 MHz are generated using a vector signal generator (VSG). The Ka-band modulated signal and the reference signal are obtained using a frequency synthesiser (FS) and two up-converters. The demodulated signal constellation can be directly visualized using two differential amplifiers (DA) and a digital oscilloscope (DO).

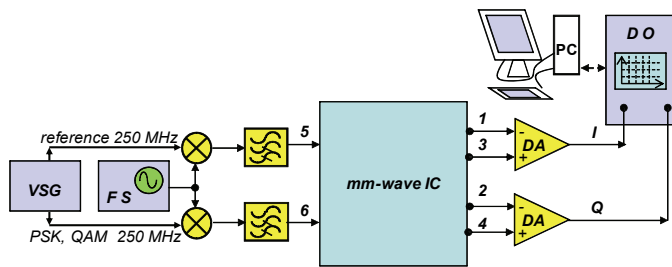


Fig. 27. Block diagram of a direct conversion measurement set-up

A detail of the fabricated prototype is illustrated in Fig. 28. The MHMICs six-port is in the center of the image. Rigid cables with Ka or SMA connectors are used to connect all front-end components. A separate board includes two differential amplifiers connected to the oscilloscope inputs.

Various demodulated constellations were obtained using the Ka-band test bench. As an example, Figs. 29 and 30 show image captures of the demodulated quadrature signals for 8PSK and 16 QAM, respectively. Other signals, such as BPSK or QPSK can be considered particularly cases.

The digital real time oscilloscope in YT display format was used to capture the images.

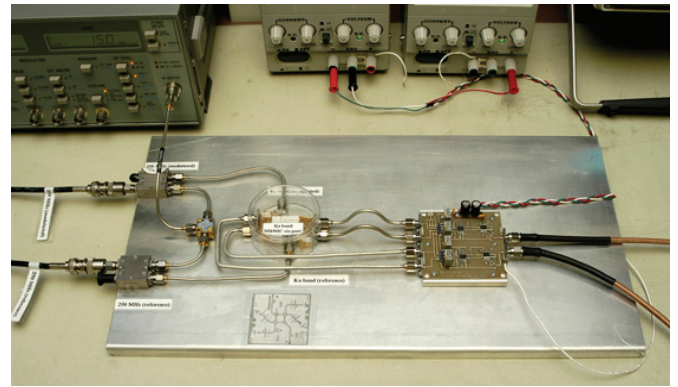


Fig. 28. Radar front-end connected to the measurement set-up

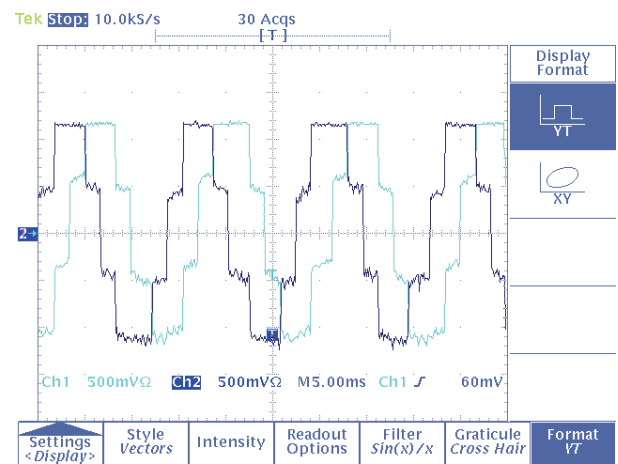


Fig. 29. Quadrature outputs for 8 PSK demodulation

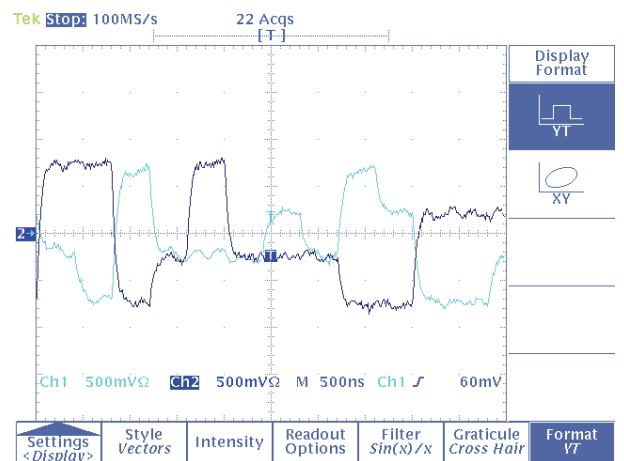


Fig. 30. Quadrature outputs for 16 QAM demodulation

Figs. 31 and 32 show image captures of the demodulated quadrature signals for 8PSK and 16 QAM, respectively.

The digital real time oscilloscope in XY display format was used to capture the images.

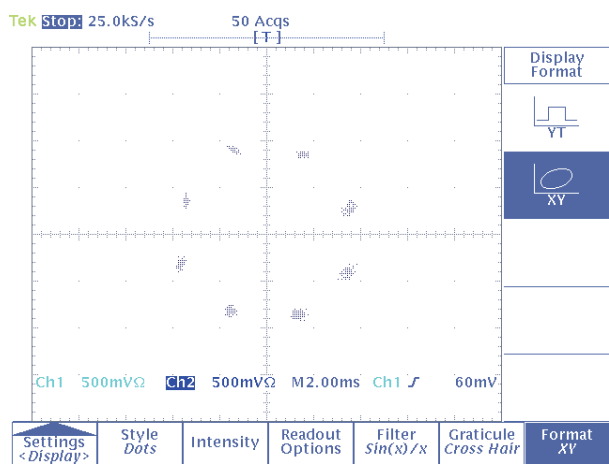


Fig. 31. Demodulated 8 PSK constellation using six-port

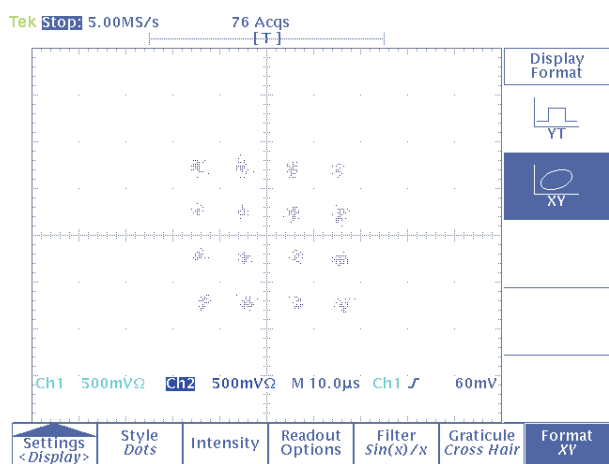


Fig. 32. Demodulated 16 QAM constellation using six-port

Fig. 33 shows real time dynamic transition from BPSK to QPSK, 8PKS and 16 QAM.

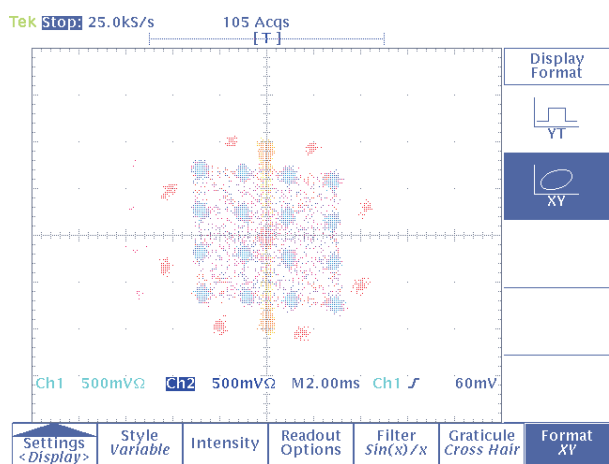


Fig. 33. Demodulated signals from BPSK to 16 QAM

Phase adjustments were not made to the front-end reference port during this process, proving the robustness and accuracy of the six-port demodulator.

To conclude our experiences with Ka-band six-port direct demodulator, the RF input power was modified in 4 dB steps. The results are shown in Fig. 34. The image was captured on the oscilloscope screen, with 10 s image persistence.

We can see that the constellation radius increases with two steps of around 4 dB, corresponding to -24 dBm, -20 dBm, and -16 dBm RF input power at port 6. The second circle radius is around 1.6 times more than initial radius, corresponding to a gain of 4 dB. The third circle radius is around 2.5 times more than initial radius (a gain of 8 dB).

As well, each demodulated cluster keeps the appropriate phase with a minimal error. This experiment demonstrates the ability of the six-port to demodulate modern modulation schemes, such as star QAM, which cannot be generated by our vector generator.

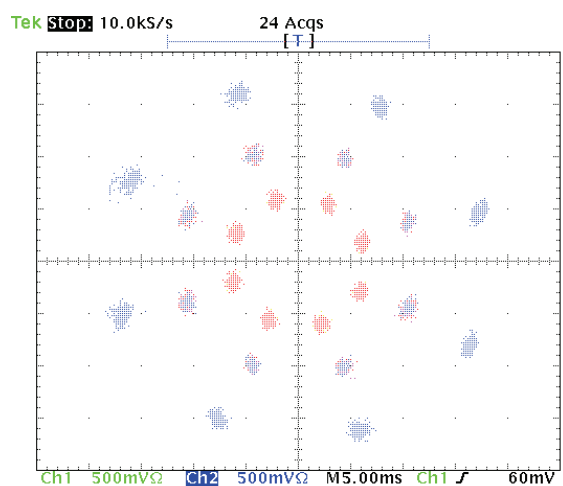


Fig. 34. 8 PSK constellation radius versus the input power

Previous measurement results prove, once again, that real time demodulation, without any six-port calibration can be performed with good precision using the six-port technology. Best bit error rates are obtained for relative simple modulation schemes, which keep a safe distance between symbols.

The second example of system measurements is the E-band radar sensor.

A photo of the millimetre-wave radar front-end is presented in Fig. 35. The 3 dB rectangular waveguide brass coupler is used to split the 77 GHz FMCW signal through the reference input of the six-port receiver (port 2) and the conical horn antenna of 20 dBi gain (port 3).

Heterodyne radar sensor architecture is investigated, according to the test bench of Fig. 36. In the transmitter part, the 77 GHz FMCW signal is generated using a function generator (FG), connected to the frequency synthesiser (FS).

In this experiment, the repetition frequency of the triangular signal is $1/T = 80$ kHz, and the frequency deviation $\Delta f = 240$ MHz.

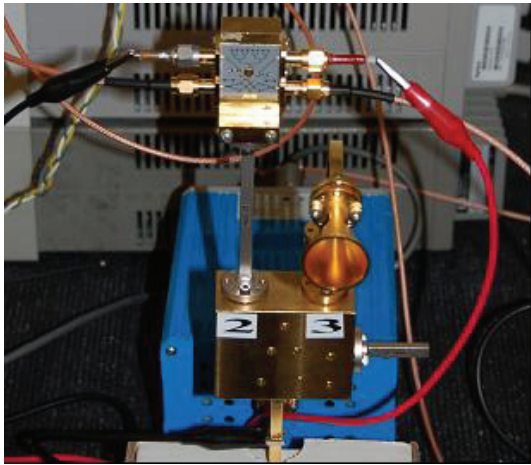


Fig. 35. Radar front-end connected to the measurement set-up

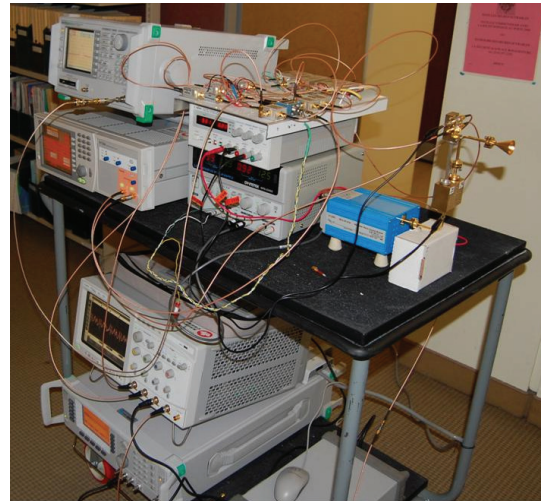


Fig. 37. Test bench of 77 GHz radar sensor

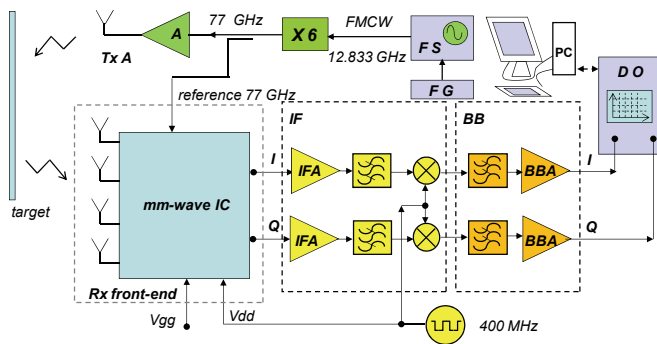


Fig. 36. Block diagram of radar front-end

The millimetre-wave amplifier (A) can be interconnected between the port 3 of the coupler and the transmitter horn antenna (Tx A), for a longer-range operation.

In the receiver part, the multi-port receiver quadrature output signals are amplified and down-converted to the baseband using conventional circuitry, such as IF amplifiers (IFA), filters, mixers, and baseband amplifiers (BBA).

It is to be noticed that the use of 400 MHz square-wave generates $77 \text{ GHz} \pm \text{IF}$ signals at LNA output. Therefore, a 400 MHz IF quadrature signal is produced at millimetre-wave IC output.

The quadrature signals generated by the receiver front-end are amplified using intermediary frequency amplifiers (IFA), and then filtered, down-converted, filtered once again, amplified in the baseband module (BBA) and, finally, visualized on a digital oscilloscope (DO) or a spectrum analyzer screen.

Indoor range measurements using the millimetre-wave hybrid prototype (rectangular waveguide transmitter and integrated MHMICs receiver) are carried out.

Fig. 37 shows the complete test bench implemented according to the previous block diagram. We note that our efforts have been focused in the design of the millimetre-wave front-end. The IF and BB circuits uses standard modules from Mini Circuits, which can be further integrated for a compact prototype.

Relative error magnitudes related to the FMCW range estimation are shown in Fig. 38. As expected, these errors are slightly increased in the vicinity of the target and decrease with the distance, up to a certain level. Multiple reflections occur between the target and laboratory equipments, increasing the measurement error for certain range values. It must also to be considered that the signal to noise ratio degrades with respect to the distance, too.

To conclude our experiment analysis, the relative error related to range measurement is considered acceptable for the proposed radar sensor dedicated to low-cost automotive applications.

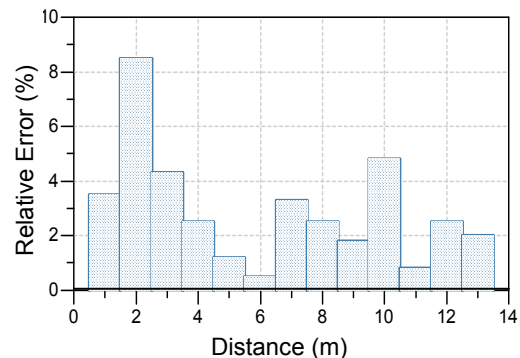


Fig. 38. Relative error for indoor range measurements

IX. CONCLUSION

An overview of basic theoretical aspects of six-port theory and techniques is presented in the beginning of the paper. The authors use the same circuit architecture to confirm once again that, once designed, the six-port can be used without any internal modification to build, for example, but not limited to, high performance quadrature down-converters, direct modulators, direction finding circuits or similar functional modules. The use of ports and the modules connected to them will change the role/function played in a system.

A chronological review of fabrication technologies used in circuit prototyping by our research team is further presented.

Even if the six-ports were designed from as low as 250 MHz, the examples covered by this paper are in the higher microwave or millimetre-wave spectrum. This represents, without any doubt, a challenge in the design, fabrication, and characterisation of the circuits.

A mature fabrication technology for low-cost circuit prototyping, combining the use of RWG, when needed, with planar integrated circuits fabricated in MHMIC and MMIC technology, is illustrated in the case of a 77 GHz front-end for radar sensor applications.

The use of MHMIC technology in the 60 - 90 GHz spectrum requires the use of very thin alumina substrate, combined with higher impedances transmission lines, when required. The thickness of the substrate is compatible with the one of MMIC circuits, ensuring wire-bonding compatibility.

The most important rules to achieve a very good design are: (i) the layout symmetry of all circuits, from dividers and couplers to six-ports; (ii) the rounded layout, in order to avoid discontinuities, (iii) the aspect ratio of circuits considering the width, the length, and the radius of curved transmission lines.

Circuit characterisation uses a PNA and probe station. The calibration kit is integrated along with the other circuits, to ensure a high measurement precision. Several circuit designs are tested and the best one is chosen for the final prototype. Full port circuit models are extracted from multiple two port measurements, to be used in advanced system simulations.

Very good S-parameter measurements are obtained in terms of return and insertion losses, isolation, magnitude and phase imbalance, as illustrated in several examples in the paper.

The final prototype is validated by system simulation and measurements. Its mechanical design must also fit with laboratory equipment. The paper illustrated the test bench of a Ka-band direct demodulator and that of an E-band radar sensor.

We finally conclude that the six-port technology, due to its performances, is a candidate of choice in a very range of microwave and millimetre-wave front-end designs. Prototyping activities or small scale fabrications can benefit from fabrication technologies described in this paper.

ACKNOWLEDGEMENT

This is an extended version of the paper "Six-port Technology and Applications" presented at the 11th International Conference on Telecommunications in Modern Satellite, Cable and Broadcasting Services - TELSIS 2013, held in October 2013 in Niš, Serbia.

This work was supported in part by the National Science Engineering Research Council of Canada (NSERC) and "Fonds de recherche du Quebec- Nature et technologies" (FRQNT).

The authors would like to acknowledge the support of the "Centre de Recherche en Électronique Radiofréquence" (CREER) of Montreal, funded by FRQNT, for the prototypes' fabrication.

REFERENCES

- [1] S.B. Cohn, N.P. Weinhouse, "An automatic microwave phase measurement system," *Microwave Journal*, vol. 7, no. 2, pp. 49-56, 1964.
- [2] G.F. Engen, C.A. Hoer, "Application of an Arbitrary 6-Port Junction to Power-Measurement Problems", *IEEE Transactions on Instrumentation and Measurement*, pp. 470-474, 1972.
- [3] G.F. Engen, "The Six-Port Reflectometer an Alternative Network Analyzer", *IEEE Transactions on Microwave Theory and Techniques*, MTT-25, pp. 1075-1077, 1977.
- [4] S.O. Tatu, T. Denidni, "A New Beam Direction Finding Circuit Based on Six-Port Technology", *IEEE Microwave Theory and Techniques Symposium 2005*, Conference CD, IEEE Catalogue Number 05CH37620C, ISBN 0-7803-8846-1, Long Beach, California, USA, 2005.
- [5] S.O. Tatu, E. Moldovan, S. Affes, "Multi-Port Front-End and Transceivers for V-Band Multi-Gigabit/s Communication Systems", *Digital Front-End in Wireless Communications and Broadcasting Circuits and Signal Processing*, ISBN:9781107002135, pp. 707-732, Chapter DOI: <http://dx.doi.org/10.1017/CBO9780511744839.025>, Cambridge University Press, Cambridge, UK, 2011.
- [6] D. Hammou, N. Khaddaj Mallat, E. Moldovan, S. Affes, Ke Wu, S.O. Tatu, "V-band Six-Port Down-conversion Techniques", *International Symposium on Signals, Systems, and Electronics (ISSSE)*, conference CD, IEEE catalog Number 07EX1869C, pp. 379-382, Montreal, Canada, 2007.
- [7] S.O. Tatu, E. Moldovan, Ke Wu, R.G. Bosisio, "A New Direct Millimeter-Wave Six-Port Receiver", *IEEE Transactions on Microwave Theory and Techniques*, vol.49, no.12, pp. 2517-2522, 2001.
- [8] S.O. Tatu, E. Moldovan, G. Brehm, Ke Wu, R.G. Bosisio, "Ka Band Direct Digital Receiver", *IEEE Transactions on Microwave Theory and Techniques*, vol.50, no.11, pp. 2436-2442, 2002.
- [9] E. Moldovan, S.O. Tatu, T. Gaman, Ke Wu, R.G. Bosisio "A New 94 GHz Six Port Collision Avoidance Radar Sensor", *IEEE Transactions on Microwave Theory and Techniques*, vol.52, no.3, pp. 751-759, 2004.
- [10] B. Boukari, D. Hammou, E. Moldovan, R. G. Bosisio, Ke Wu, S.O. Tatu, "MHMICs on Ceramic Substrate for Advanced Millimeter wave Systems", *2009 IEEE Microwave Theory and Techniques Symposium*, Conference Proceedings, pp. 1025-1028, Boston, MA, USA, 2009.
- [11] S. O. Tatu, B. Boukari, E. Moldovan, R. G. Bosisio, Ke Wu, "Millimeter-wave Multi-port Radar Sensor with Integrated Receiver Front-end for Automotive Applications", *2012 IEEE Microwave Theory and Techniques Symposium*, Conference Proceedings, ISBN: 978-1-4673-1088-8/12©2012 IEEE, Montreal, Canada, 2012.
- [12] D. Hammou, E. Moldovan, S.O. Tatu, "Novel MHMIC Millimeter Wave Power Divider/Combiner", *2011 IEEE Canadian Conference on Electrical and Computer Engineering (CCECE 2011)*, Conference proceedings, pp. 280-283, Niagara Falls, Ontario, Canada, 2011.
- [13] S.O. Tatu, E. Moldovan, Ke Wu, R.G. Bosisio, T. Denidni, "Ka-Band Analog Front-end for Software Defined Direct Conversion Receiver", *IEEE Transactions on Microwave Theory and Techniques*, vol.53, no.9, pp. 2768-2776, 2005.
- [14] S.O. Tatu, B. Boukari, E. Moldovan, R. G. Bosisio, Ke Wu, "Millimeter-wave Multi-port Radar Sensor with Integrated Receiver Front-end for Automotive Applications", *2012 IEEE Microwave Theory and Techniques Symposium*, Conference Proceedings, ISBN: 978-1-4673-1088-8/12©2012 IEEE, Montreal, Canada, 2012.